

High-Curie-temperature ferromagnetism in bilayer CrI₃ on bulk semiconducting substrates

Nanshu Liu, Si Zhou^{✉,*} and Jijun Zhao

*Key Laboratory of Materials Modification by Laser, Ion and Electron Beams, Dalian University of Technology,
Ministry of Education, Dalian 116024, China*



(Received 14 May 2020; revised 18 July 2020; accepted 17 August 2020; published 15 September 2020)

Two-dimensional (2D) ferromagnetic (FM) semiconductors with high Curie temperature have long been pursued for electronic and spintronic applications. Here we provide a general strategy to achieve robust FM state in bilayer CrI₃ of the monoclinic stacking, which intrinsically has interlayer antiferromagnetic (AFM) order and weak in-plane FM coupling. We showed that the proximity effect from bulk semiconducting substrates induces electronic doping and significantly increases the FM nearest-neighbor exchange for bilayer CrI₃, leading to the AFM-to-FM transition for the interlayer spin configuration as well as enhanced intralayer FM coupling. By first-principles calculations and Monte Carlo simulations, bulk and 2D semiconductors providing different interaction strengths from strong covalent bonding to weak van der Waals (vdW) interaction with CrI₃ are compared to thoroughly address the substrate effect on magnetic behavior and Curie temperature of bilayer CrI₃. These theoretical results offer a facile route for direct synthesis of 2D ferromagnets on proper semiconducting substrates to achieve high Curie temperature for device implementation.

DOI: [10.1103/PhysRevMaterials.4.094003](https://doi.org/10.1103/PhysRevMaterials.4.094003)

I. INTRODUCTION

Two-dimensional (2D) magnetic materials have attracted tremendous attentions owing to their peculiar spin-related phenomena and immense potentials for magneto-optics, magnetoelectronics, and spintronic devices [1–5]. As a rising star of 2D ferromagnets, monolayer CrI₃ possesses many exciting features including perfect crystalline order, intrinsic Ising type ferromagnetism [6,7], strong magnetic anisotropy, and a sizable band gap of about 1.2 eV [8]. Unfortunately, the ferromagnetic (FM) coupling is rather weak in monolayer CrI₃ with a Curie temperature (T_c) of only 45 K, while bilayer CrI₃ with monoclinic stacking even exhibits antiferromagnetic (AFM) behavior with opposite magnetic moments from the neighboring FM layers [9]. Clearly the fragile magnetic order of CrI₃ susceptible to the variation of layer thickness and stacking order has greatly hindered the application of this novel 2D material.

For practical interests, large-area CrI₃ sheets on semiconducting substrates are highly desirable, and an ideal scenario for device implementation is to select proper substrates to achieve robust FM order in CrI₃ ultrathin films. Currently, monolayer and multilayer CrI₃ can be synthesized by the exfoliation method and then transferred to insulating substrates, as well as be epitaxially grown on metal and nonmetal substrates, such as gold [10], highly oriented pyrolytic graphite (HOPG) [6], and yttrium stabilized zirconia [11]. Generally speaking, most 2D materials as substrates provide van der Waals (vdW) interaction with CrI₃ and can either retain or slightly perturb its intrinsic electronic band structure. In contrast, bulk materials with polar surface and dangling bonds

may covalently couple to CrI₃, resulting in some exotic functionalities at the interfaces. Therefore, appropriate choice of substrates enables a large degree of freedom for band structure engineering of 2D CrI₃ and may give rise to unprecedented device architectures.

Previous studies have explored the proximity effect in several CrI₃-based vdW heterostructures. In experiment, the heterostructure of monolayer WSe₂ and few-layer CrI₃ has been exploited for valley manipulation of WSe₂ through control of the magnetization in CrI₃ [12]; in turn, the spin-valley properties render WSe₂ a magnetic sensor for mapping out the layered antiferromagnetic domain in the CrI₃ sheet [13,14]. On the theoretical aspect, the mechanism for valley splitting in WSe₂/CrI₃ heterostructures has been elucidated by considering the effects of stacking geometry [15], electrical field [16], and intrinsic point defects in CrI₃ [17]. Quantum anomalous Hall effect was also proposed by coupling Bi₂Se₃ or MnBi₂Te₄ with CrI₃ monolayer, which induces sizable spin splitting of the topological states [18,19]. Moreover, it was predicted that the in-plane FM coupling of CrI₃ monolayer can be enhanced with T_c up to 85 K when supported on MoTe₂ [20], silicene, and germanene monolayers [21], owing to spin-dependent charge transfer at the heterojunctions and introduction of extra spin superexchange path.

Directly growing or relocating CrI₃ sheet on proper substrates for magnetism engineering can overcome the limitations inherent to doping, functionalization, and applying external fields, which may result in unintended clustering, disorder, or phase transition. However, current understanding of the proximity effect in CrI₃ is based only on the aforementioned vdW heterostructures. How does the interlayer exchange of CrI₃ vary with the bonding nature and strength of substrate? Is it possible to retain the magnetic order and semiconducting character of CrI₃ covalently bound on a

*Corresponding author: sizhou@dlut.edu.cn

bulk substrate? Is there an optimal CrI₃-substrate interaction strength that leads to robust FM coupling between CrI₃ layers and high T_c for practical uses? These intriguing questions are all waiting to be solved.

In this work we explored bilayer CrI₃ on a variety of nonmetal substrates with a wide range of interfacial coupling strength, including bulk semiconductors (II-VI compounds, silicon) as well as 2D monolayer materials (group III and group IV monochalcogenides, transition metal dichalcogenides, phosphorene, etc.). By first-principles calculations, the geometries, electronic band structures, and magnetic behavior of the supported CrI₃ sheet were systematically investigated. Strong FM order of bilayer CrI₃ with T_c above 130 K was realized on selected bulk substrates, and the underlying exchange mechanism was elucidated. We further determined the key parameters that govern the exchange energy of bilayer CrI₃ on various substrates, paving a way for precisely modulating the magnetism of CrI₃ ultrathin sheets.

II. COMPUTATIONAL METHODS

The structure, electronic, and magnetic properties of bilayer CrI₃ on various substrates were investigated by density functional theory (DFT) calculations implemented in the Vienna *ab initio* simulation package (VASP) [22]. We adopted the plane-wave basis set with energy cutoff of 500 eV, projected augmented wave (PAW) potentials for electron-ion interaction [23], and generalized gradient approximation parametrized by Perdew, Burke and Ernzerhof (GGA-PBE) for the exchange and correlation functional [24]. Grimme's semiempirical DFT-D3 scheme for dispersion correction was employed to describe the van der Waals (vdW) interactions between CrI₃ layers and substrate [25]. Our test calculations show that the choice of vdW functionals may affect the absolute value of interlayer exchange energy (E_M) defined by Eq. (2), but give the same trend of E_M for different heterostructure systems (Table SI of the Supplemental Material, SM [26]). Moreover, the ground state of freestanding bilayer CrI₃ of the high-temperature (HT) phase is correctly predicted to be antiferromagnetic by using PBE-D3, vdW-optB86b, and vdW-PBE functionals, all consistent with the previous theoretical results based on PBE-D3 [27]. A Hubbard on-site Coulomb parameter $U = 3.0$ eV was chosen for Cr atoms to account for the strong correlation effect, which can correctly predict the antiferromagnetic state for freestanding bilayer CrI₃ in the monoclinic stacking according to our calculations (see Fig. S1 of the SM for details [26]) as well as the previous theoretical study [28].

The supercells for bilayer CrI₃ on various substrates have lateral dimensions (L) of 6.76–21.20 Å and a vacuum space of 15 Å in the out-of-plane direction (Table SII). The details of how to construct the heterostructure models are described in Fig. S2 of the Supplemental Material [26]. Among the substrates, the II-VI semiconductors ZnO, ZnS, and CdSe of wurtzite phase with the exposed (0001) surface were modeled by a four-layer slab, and the bottom-layer chalcogen atoms were terminated by H atoms. The in-plane lattice of CrI₃ sheet was slightly stretched or compressed to fit that of the substrate (with lattice mismatch below 1.3%) to ensure that the strain effect on the magnetic properties of CrI₃ sheet is negligible

compared with the substrate effect. The Brillouin zones of the supercells were sampled by the Monkhorst-Pack \mathbf{k} -point meshes with a separation of 0.01 \AA^{-1} . With fixed supercells, all the model structures were fully relaxed for the ionic and electronic degrees of freedom with convergence criteria of 10^{-5} eV for energy and 0.02 eV/\AA for force, respectively. The charge transfer between CrI₃ sheet and substrate was evaluated by the Bader charge analysis [29].

III. RESULTS AND DISCUSSION

We considered bilayer CrI₃ with the monoclinic lattice and $C2/m$ space group symmetry, which is the HT phase observed in experiment at 210–220 K. It is formed by two CrI₃ layers in AA stacking with one layer sliding by $a/3$ along the in-plane lattice vector \mathbf{a} with respect to the other [Figs. 1(a) and 1(b)]. Within CrI₃ monolayer, each Cr atom is coordinated by six I atoms with the Cr–I–Cr bond angle close to 90° , resulting in the FM coupling according to the superexchange theorem [30–32]. The magnetic moment is $3\mu_B$ per Cr atom, and the band gap is 1.17 eV predicted by the PBE functional, as revealed by the electronic band structure and density of states (DOS) in Fig. 1(c). Under the octahedral crystal field, the d orbitals of Cr atoms split into threefold occupied t_{2g} (d_{xy} , d_{yz} , and d_{xz}) orbitals and twofold unoccupied e_g (d_z^2 and $d_{x^2-y^2}$) orbitals, corresponding to t_{2g} (d_{xy} , $d_{x^2-y^2}$, and d_z^2) and e_g (d_{yz} and d_{xz}) orbitals in the present coordination system. By stacking two CrI₃ layers into the HT phase, e_g or t_{2g} states in one layer for a given spin channel is degenerate with the same band of opposite spin in the other layer [33], leading to antiferromagnetic order [Fig. 1(d)]. Our calculations show that the AFM state of bilayer CrI₃ is slightly lower in energy than the FM state by -0.24 meV per CrI₃ formula unit (f.u.), consistent with the previous experimental observation and theoretical reports (-0.20 meV/f.u. [6,34–36]). As displayed by Fig. 5(c) (AFM1), the spin moments align ferromagnetically within each CrI₃ layer but point to the opposite directions between the layers. This is because the interlayer FM coupling is dominated by the virtual excitation from t_{2g} to e_g orbital, which encounters a large energy separation of 1.33 eV and cannot compete with the AFM exchange governed by interlayer e_g - e_g and t_{2g} - t_{2g} hybridization [27].

To enhance the e_g - t_{2g} interaction and achieve robust FM order in bilayer CrI₃, we take advantage of the proximity effect by placing the CrI₃ sheet on a suitable substrate. To explore the specific influence of substrate interaction on the magnetic state of the supported CrI₃ bilayer, we considered a variety of substrate materials, including (0001) surface of II-VI wurtzite compounds CdSe, ZnS, and ZnO, bulk Si(111) surface, 2D group III monochalcogenide GaSe and InSe, 2D group IV monochalcogenide SnS, 2D transition metal dichalcogenide MoS₂ and WSe₂, phosphorene (black P), and *h*-BN. The geometrical structures of these hybrid systems are displayed in Fig. S3 [26]. For clarity, we define the bottom CrI₃ layer close to the substrate as the first layer, and the top one as the second layer. The interaction between the CrI₃ sheet and a substrate is characterized by the interfacial binding energy (E_{bind}) defined as

$$E_{\text{bind}} = (E_{\text{tot}} - E_{\text{CrI3}} - E_{\text{sub}})/N_{\text{Cr}}, \quad (1)$$

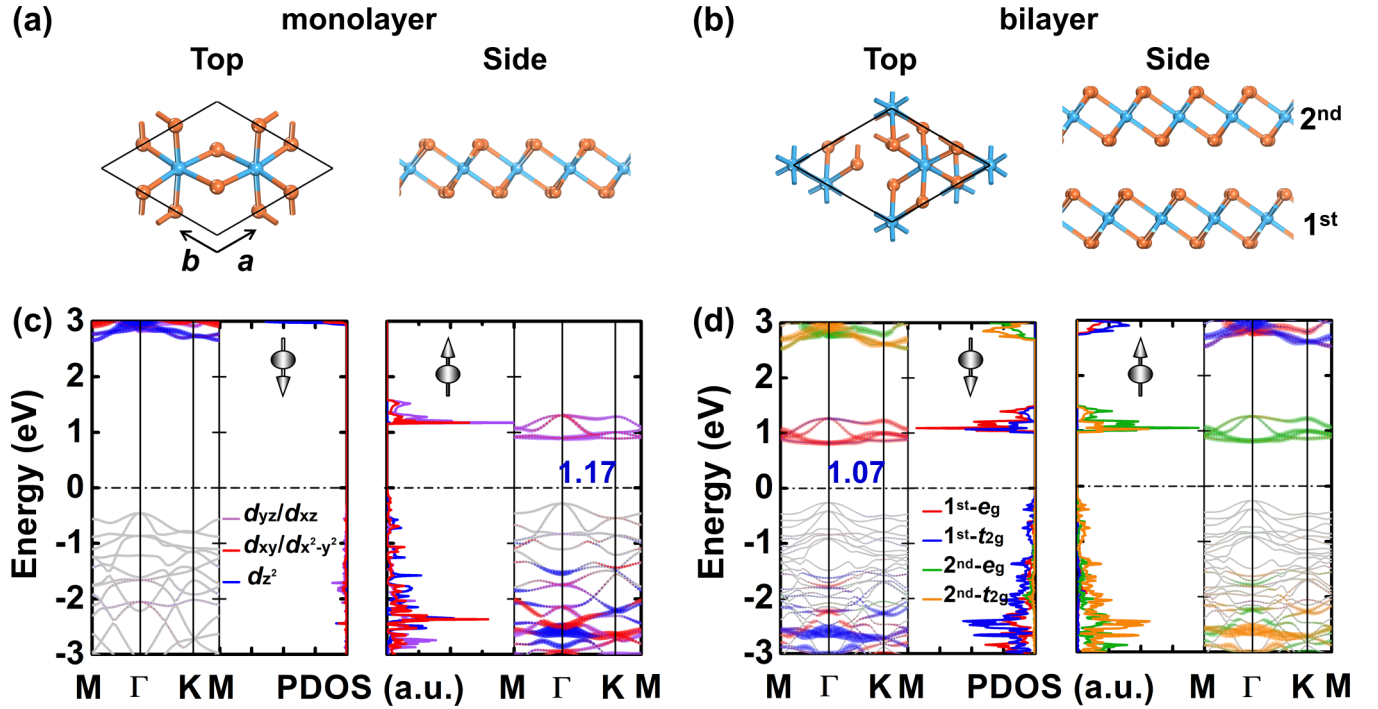


FIG. 1. Atomic structures (top and side views) and spin-polarized electronic band structures along with projected density of states (PDOS) of monolayer (a) and (c) and bilayer (b) and (d) CrI_3 , respectively. The Cr and I atoms are shown in blue and orange colors, respectively. \mathbf{a} and \mathbf{b} are the lattice vectors. The colored lines in bands and PDOS are from d orbitals of Cr atoms. The blue numbers give the band gap (in eV) for each system. The Fermi level (dashed lines) is set to zero. On each panel of PDOS, the spin orientation is given by an up or down arrow.

where E_{CrI_3} and E_{tot} are the energies of freestanding and supported bilayer CrI_3 , respectively; E_{sub} is the energy of the standalone substrate; and N_{Cr} is the number of CrI_3 formula units (f.u.) in monolayer CrI_3 within the supercell model (which equals to the number of Cr atoms at the interface with substrate). The interlayer distance d is defined as the average vertical distance between the bottom I layer of CrI_3 and the substrate surface.

As revealed by Table I, the CrI_3 bilayer exhibits strong interaction with the II-VI semiconductor surfaces, having interlayer distances of 2.13–2.59 Å and E_{bind} ranging from –2.32 to –4.48 eV/f.u., while the geometric structure of

the supported CrI_3 sheet remains almost the same as that of the freestanding bilayer (see the geometrical parameters in Table SII [26]). At the interface, the I atoms of CrI_3 form covalent bonds with the surface metal atoms of the substrate, accompanied by charge transfer (CT) of 0.24–0.41 e/f.u. from substrate to CrI_3 . Accordingly, differential charge density in Fig. 4(d) shows notable electron accumulation in the interfacial region. On the Si(111) surface, the substrate interaction is relatively weaker with $E_{\text{bind}} = -1.76$ eV/f.u. and $\text{CT} = 0.19$ e/f.u., while vdW interaction is found between CrI_3 layer and all the considered 2D materials, manifested by their large interlayer distance (3.18–3.69 Å) as well as small

TABLE I. Structural and magnetic properties of bilayer CrI_3 on various substrates, including lattice mismatch (δ), average interlayer distance between CrI_3 and substrates (d), interlayer binding energy (E_{bind}), work function of substrates (Φ) (experimental values in brackets), charge transfer (CT) from substrates to CrI_3 , interlayer exchange energy (E_M), intralayer exchange energy for the bottom CrI_3 layer ($E_{M||}$), and the associated exchange parameters (J).

System	δ (%)	d (Å)	E_{bind} (eV/f.u.)	Φ (eV)	CT (e/f.u.)	E_M (meV/f.u.)	$J_{1\perp}$ (meV)	$J_{2\perp}$ (meV)	$E_{M }$ (meV/f.u.)	$J_{1 }$ (meV)	$J_{2 }$ (meV)
CdSe(0001)	0.90	2.58	–4.48	3.81(3.72 [38])	0.24	9.42	6.32	–1.76	43.31	6.42	3.69
ZnS(0001)	0.79	2.59	–2.46	3.68(4.10 [39])	0.30	5.59	8.19	–1.71	41.41	6.13	1.62
ZnO(0001)	0.12	2.13	–2.32	3.60(3.70 [40])	0.41	5.04	6.51	–2.43	38.16	5.65	1.04
Si(111)	0.32	2.28	–1.76	4.58(4.40 [41])	0.19	3.26	9.19	–4.00	37.29	5.52	4.15
SnS	1.16	3.29	–0.41	4.33	0.06	1.08	2.84	–0.61	33.96	5.03	1.28
MoS ₂	0.46	3.42	–0.38	5.70	–0.03	0.09	1.05	–0.41	22.28	3.30	1.37
WSe ₂	0.51	3.55	–0.39	4.91	0.01	0.08	0.44	–0.17	28.38	4.20	1.72
GaSe	0.58	3.49	–0.29	5.64	–0.08	0.06	5.43	–2.40	18.52	2.74	1.20
<i>h</i> -BN	0.31	3.60	–0.28	5.57	0.01	–0.06	–1.21	2.71	19.06	2.82	1.23
Black P	1.27	3.44	–0.34	4.90(5.04 [42])	0	–0.08	–10.27	4.55	28.85	4.27	2.48
InSe	1.30	3.18	–0.35	5.75	–0.04	–0.30	–19.78	0.91	17.14	2.54	1.36

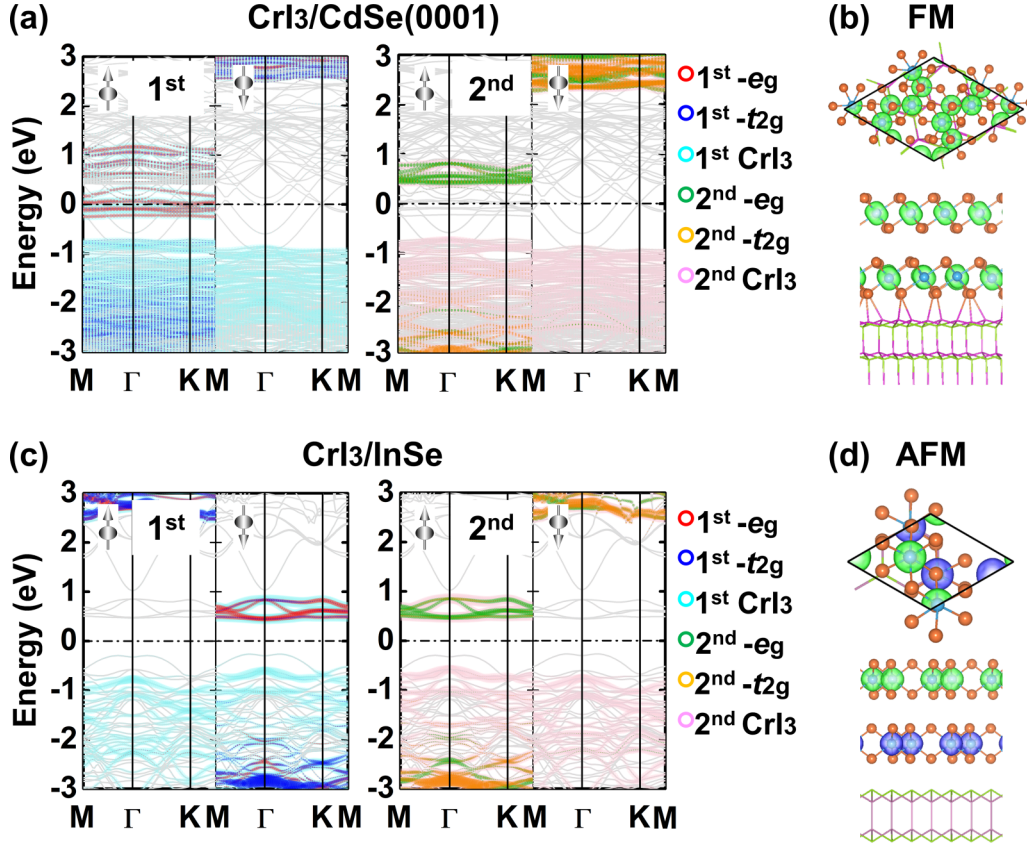


FIG. 2. Spin-polarized band structures of bilayer CrI_3 on (a) $\text{CdSe}(0001)$ and (c) 2D InSe , respectively. Left panel: First CrI_3 layer (cyan), right panel: second CrI_3 layer (magenta); the bands from substrates are shown in light gray; the projected bands from e_g and t_{2g} orbitals are given in the other colors. The Fermi level (dashed lines) is set to zero. The spin densities of the ground states are shown in (b) and (d). The spin up and spin down components (labeled by arrows) are shown in green and blue colors, respectively, with an isosurface value of $0.01 \text{ e}/\text{\AA}^3$.

E_{bind} (-0.28 to -0.41 eV/f.u.) and CT ($\leq 0.06 \text{ e/f.u.}$). For all the systems, the monoclinic stacking of bilayer CrI_3 is well retained, and the optimized structures of supported CrI_3 sheets do not show any reconstruction owing to the small lattice mismatch with various selected substrates. However, the exchange interaction between two CrI_3 layers is effectively modulated by the substrate, and consequently the preferred magnetic order of bilayer CrI_3 would be modified as will be discussed in the following.

The band structures and DOS of bilayer CrI_3 on various substrates are presented in Fig. 2 and Fig. S4 [26], respectively. Significant changes to band structure have been induced by the four bulk semiconductor substrates, while the 2D materials with vdW interaction only shift the bands of CrI_3 by some extent. Taking bilayer CrI_3 on $\text{CdSe}(0001)$ as an example [Figs. 2(a) and 3(d)], the spin-down channel remains insulating. For the spin-up channel, the top CrI_3 layer presents a band gap of 1.18 eV , while the bottom CrI_3 layer strongly coupled to the substrate shows prominent impurity states near the Fermi level, resembling the band structure character of n -doped CrI_3 [8]. The substrate-induced doping introduces itinerant carriers, giving rise to a half-metallic state for the supported bilayer CrI_3 . The $e_g\uparrow$ orbital of the bottom CrI_3 layer gets closer to the $t_{2g}\uparrow$ orbital of the top layer. Due to the enhanced FM e_g - t_{2g} hybridization, bilayer CrI_3 on the bulk semiconductors favor a FM ground state.

To characterize the magnetic coupling strength, we calculate the interlayer exchange energy as the energy difference between the interlayer AFM and FM spin configurations:

$$E_M = (E_{\text{AFM}} - E_{\text{FM}})/N_{\text{Cr}}, \quad (2)$$

where a negative value of E_M indicates an AFM ground state. As given by Table I, the strongest FM order is obtained for the bilayer CrI_3 sheet on $\text{CdSe}(0001)$ with $E_M = 9.42 \text{ meV/f.u.}$, almost 40 times of the magnitude of the AFM coupling for freestanding bilayer CrI_3 ($E_M = -0.24 \text{ meV/f.u.}$), signifying much enhanced FM coupling due to substrate interaction. The other semiconductor surfaces like $\text{ZnS}(0001)$, $\text{ZnO}(0001)$, and $\text{Si}(111)$ also endow FM spin configuration to bilayer CrI_3 with $E_M = 3.26$ – 5.59 meV/f.u. On some 2D materials including SnS , GaSe , MoS_2 , and WSe_2 , the vdW interaction causes remarkable shift of the bands of CrI_3 , i.e., the Fermi level approaching the bottom of conduction band, while the band gap is slightly reduced to 0.44 – 0.96 eV , leading to relatively weak FM order with $E_M = 0.06$ – 2.00 meV/f.u. On the rest of the 2D materials like InSe , black P, and h -BN, the band gap of the CrI_3 sheet is almost intact, and the interlayer AFM coupling is maintained with $E_M = -0.06$ to -0.30 meV/f.u.

For the substrates providing vdW interaction, we further explored strategies to strengthen the interlayer ferromagnetic order of bilayer CrI_3 on the vdW substrate. We considered

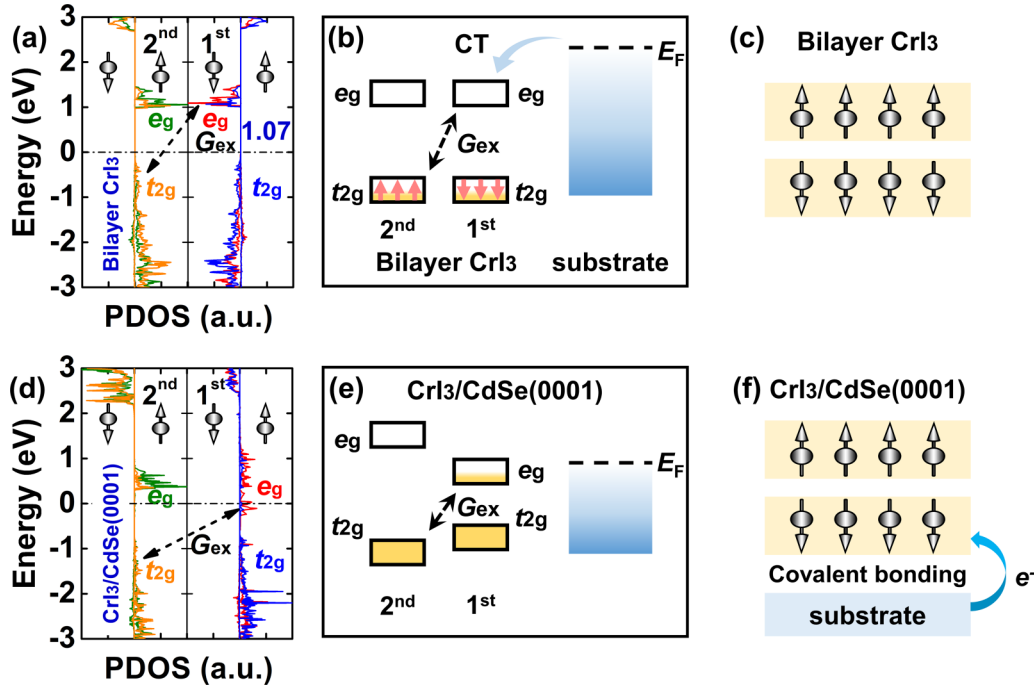


FIG. 3. (a) and (d) Projected density of states (PDOS) from the e_g and t_{2g} orbitals of freestanding bilayer CrI₃ and that on CdSe(0001) surface, respectively. On each panel of PDOS, the spin orientation is given by an up or down arrow. The schematic illustrations of orbital alignments (b) and (e) and spin configurations (c) and (f) are shown for each system.

bilayer CrI₃ on graphene (lattice mismatch is 0.38%) as a representative system feasible in the experiment and obtained $E_M = 2.31$ meV/f.u., compared with $E_M = -0.24$ meV/f.u. for freestanding CrI₃ bilayer with AFM order. This means that an AFM-to-FM transition can be realized by placing bilayer CrI₃ on graphene as a vdW substrate. By applying an external electric field perpendicular to the CrI₃ sheet, E_M further increases to 2.93 meV/f.u. at $F = 0.2$ V/Å (see Fig. S5(a) [26]). Moreover, considering the possible in-plane strain in CrI₃ bilayer supported on a certain substrate due to lattice mismatch, we examined the effect of biaxial strain on the magnetism of freestanding bilayer CrI₃. As shown in Fig. S5(b) [26], the freestanding system remains AFM under stretching strain, while it switches to the FM state under compressive strain larger than 4%. In particular, E_M reaches 0.45 meV/f.u. under 5% compressive strain. Therefore, by depositing HT-phase CrI₃ bilayer on a suitable vdW substrate to induce proper in-plane strain and meanwhile by applying a vertical electric field, it is possible to significantly enhance the interlayer FM order and raise the Curie temperature for device application.

The AFM to FM transition in bilayer CrI₃ is attributed to its electron transfer with the substrate, which alters not only the energy level but also the occupancy of e_g orbital of the bottom CrI₃ layer, as illustrated by Fig. 3. The e_g - t_{2g} interaction strength that dominates the FM coupling of CrI₃ layers can be reflected by the virtual exchange gap (G_{ex}) between the e_g and t_{2g} orbitals. Generally speaking, the stronger CrI₃-substrate binding associated with the larger interfacial charge transfer results in the smaller G_{ex} and thus larger E_M as well as stronger FM order, as displayed in Fig. 4(a). In particular, bilayer CrI₃ on II-VI semiconductors and Si(111) surface have G_{ex} value reduced to 0.52–0.87 eV, which is a

significant impact on the electronic band structures, while 2D vdW substrates only induce band shifting and perturbation to the e_g - t_{2g} interaction ($G_{ex} = 1.10$ – 1.44 eV, compared with 1.33 eV for the freestanding system). Moreover, the electrons transferred from the substrate occupy the e_g orbitals of the bottom CrI₃ layer, and the corresponding occupancy can be calculated by

$$N_{occ.} = \frac{\int_{-\infty}^{E_F} D_{e_g}^s(E) dE}{\int_{-\infty}^{+\infty} D_{e_g}^s(E) dE}, \quad (3)$$

where $D_{e_g}^s(E)$ is the density of states from the e_g orbitals of the bottom CrI₃ layer at a given energy E . Remarkably, for bilayer CrI₃ sheets on the bulk semiconductors, the considerable charge transfer leads to the occupation of e_g orbitals to be $N_{occ.} = 6.03\%$ – 12.60% (Table SII), while the freestanding bilayer and that on 2D vdW substrates have small CT < 0.06 e/f.u. and thus $N_{occ.} = 0$. As shown in Fig. 4(b), E_M generally increases with $N_{occ.}$, as larger occupation of the e_g orbital of the bottom CrI₃ layer corresponds to more substrate-induced itinerant electron carriers, and thus leads to enhanced stability of interlayer FM spin configuration against AFM one.

The interfacial charge transfer between bilayer CrI₃ and substrate can be correlated with the work function (Φ) of the substrate. As illustrated by Figs. 4(c) and 4(d), the substrates with lower Φ result in larger CT to the CrI₃ sheet, accompanied by stronger interfacial binding and smaller interlayer distance ($d < 2.60$ Å), which in turn leads to the increase of E_M for interlayer FM exchange. In particular, the (0001) polar surfaces of bulk II-VI semiconductors have a much smaller theoretical work function of 3.60–3.81 eV than that of 5.63 eV for freestanding bilayer CrI₃, thereby inducing

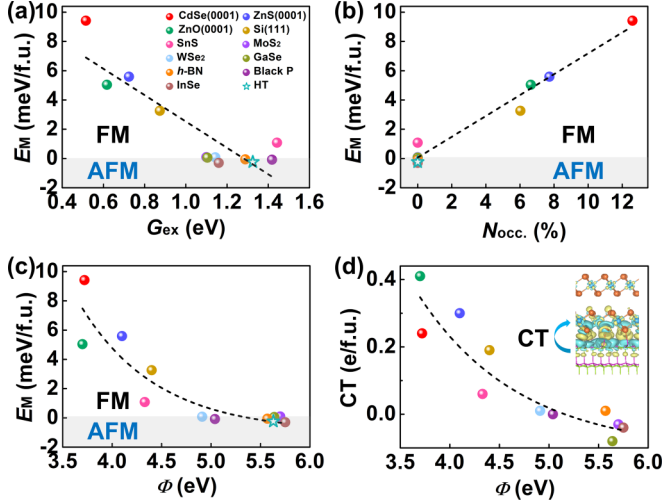


FIG. 4. (a)–(c) Interlayer FM exchange energy (E_M) of bilayer CrI_3 on various substrates as a function of virtual exchange gap (G_{ex}), occupancy of e_g orbital ($N_{\text{occ.}}$), and work function (Φ) of substrates, respectively. The values of freestanding bilayer CrI_3 in high temperature phase (denoted as HT) are also given. (d) Interfacial charge transfer (CT) vs Φ , with the inset showing differential charge densities between bilayer CrI_3 and substrate. Yellow and cyan colors represent the charge accumulation and depletion regions, respectively, with an isosurface value of $2 \times 10^{-4} e/\text{\AA}^3$.

prominent charge transfer through formation of the interfacial covalent bonds. In contrast, 2D materials have relatively larger work function in the range of 4.33 to 5.75 eV, and they donate to or even gain a small amount of electrons from the CrI_3 sheet. Therefore, they have less impact on the magnetic order in bilayer CrI_3 . In other words, by choosing proper substrates based on the work function, it is possible to control the amount of charge transfer to bilayer CrI_3 and tune the e_g - t_{2g} hybridization, ultimately modulating the interlayer spin configuration and exchange energy of the bilayer CrI_3 sheet.

To gain deeper insights into the mechanism of enhanced interlayer ferromagnetism of CrI_3 , we considered a Heisenberg model with the following Hamiltonian:

$$H = - \sum_{ij} J_{ij} M_i M_j, \quad (4)$$

where M_i and M_j represent the magnetic moments at sites i and j , respectively, and we used the computed magnetic moments for each CrI_3 /substrate model from DFT calculations (see Table SII in the SM for the values of M [26]); J_{ij} is the exchange parameter between sites i and j . Later, we will use the subscript \perp and \parallel to denote the interlayer and intralayer exchange parameters, respectively. As illustrated by Fig. 5(b), a total of five Cr–Cr neighbors in bilayer CrI_3 are considered—three for in-plane direction and two for vertical direction (the latter includes four nearest neighbors and four second nearest neighbors). The five lowest-energy AFM spin configurations are determined for freestanding and supported bilayer CrI_3 , as displayed in Fig. 5(c) and Fig. S6 [26]. According to the exchange energies of these AFM states, J_{ij} can be calculated by Eq. (4) (see Eqs. (S1)–(S12) in the SM for more details [26]). For freestanding CrI_3 bilayer, we obtained the interlayer

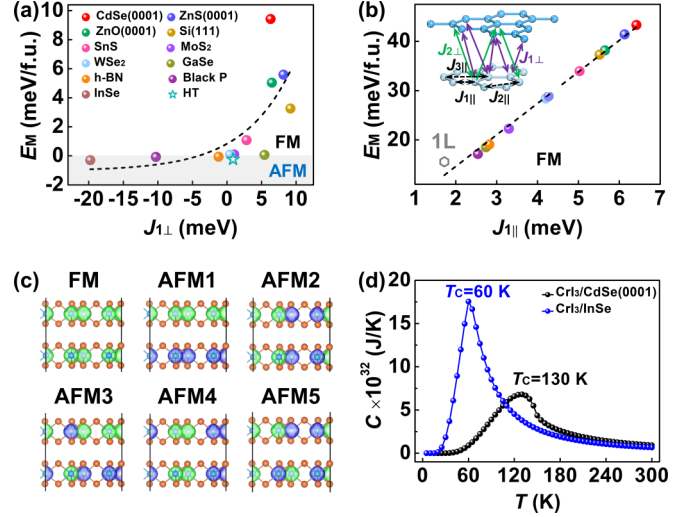


FIG. 5. (a) Interlayer FM exchange energy (E_M) of supported bilayer CrI_3 as a function of the interlayer nearest-neighbor exchange parameter (J_{\perp}). The values of freestanding bilayer CrI_3 in high temperature phase (denoted as HT) are also given. (b) Intralayer FM exchange energy ($E_{M\parallel}$) of the bottom CrI_3 layer on substrates as a function of the intralayer nearest-neighbor exchange parameter (J_{\parallel}). The inset displays the five intralayer and interlayer Cr–Cr near neighbors and the corresponding exchange parameters (J). (c) Spin densities of the five lowest-energy AFM states in freestanding bilayer CrI_3 . The spin up and spin down components are shown in green and blue colors, respectively, with an isosurface value of $0.01 e/\text{\AA}^3$. (d) Specific heat (C) as a function of temperature from Monte Carlo simulation for bilayer CrI_3 on CdSe(0001) and 2D InSe, respectively.

nearest-neighbor $J_{\perp} = 0.88$ meV representing the FM coupling, while the second nearest-neighbor $J_{2\perp} = -2.03$ meV is obtained for AFM coupling, consistent with the previous theoretical reports [27]. Upon substrate interaction, J_{\perp} is generally increased and $J_{2\perp}$ usually becomes less negative for the considered substrates, that is, stronger FM interlayer nearest-neighbor exchange and weaker AFM second nearest-neighbor exchange, which explains the enhanced interlayer FM coupling for the supported CrI_3 sheet. In particular, J_{\perp} is notably enlarged for bilayer CrI_3 on II–VI semiconductors and Si(111) surface (6.32–9.19 meV), which is about 7–10 times larger than that of the freestanding form, while $J_{2\perp}$ is less affected (−1.17 to −4.00 meV). Figure 5(a) reveals that the exchange energy E_M for the interlayer FM spin configuration increases with J_{\perp} for various supported bilayer CrI_3 systems. Therefore, the CrI_3 -substrate interaction mainly stabilizes the FM interlayer nearest-neighbor exchange term, endowing robust FM coupling between CrI_3 layers.

The substrates cannot only trigger the interlayer AFM-to-FM transition in CrI_3 , but also enhance the stability of intralayer FM state. As listed in Table I, for all the supported bilayer CrI_3 systems, the intralayer ground-state spin configuration is FM order. The bottom CrI_3 layer adjacent to the substrate has the intralayer exchange energy $E_{M\parallel} = 17.14$ –43.31 meV/f.u., compared with 16.30 meV/f.u. for the upper layer and 15.56 meV/f.u. for freestanding CrI_3 monolayer. Accordingly, the intralayer nearest-neighbor exchange parameter J_{\parallel} notably increases to 2.74–6.42 meV for

the bottom CrI_3 layer on various substrates owing to the enhanced e_g - t_{2g} hybridization ($J_{1||} = 1.72$ meV for freestanding CrI_3 monolayer). The second nearest-neighbor $J_{2||}$ is also FM and overall has less change with respect to that of freestanding CrI_3 monolayer ($J_{2||} = 1.54$ meV). Considering two in-plane Cr–Cr near neighbors in Eq. (4), the exchange energy $E_{M||}$ of intralayer FM order follows a linear relation with $J_{1||}$ for the bottom CrI_3 layer on substrate, as revealed by Fig. 5(b).

Since bilayer CrI_3 involves two macroscopic spins [34], the energy required to flip a spin requires overcoming not only the interlayer exchange energy, but also the intralayer exchange energy. Therefore, the enhancement of both in-plane and vertical FM coupling for CrI_3 bilayer on semiconducting substrates would effectively elevate the Curie temperature. Based on the calculated exchange parameters J_{ij} for both interlayer and intralayer spin configurations, we performed Monte Carlo simulations to estimate the Curie temperature of two representative systems, i.e., bilayer CrI_3 on CdSe(0001) and 2D InSe. The specific heat (C) was computed based on the Heisenberg model, and the peak on $C(T)$ curve corresponds to the temperature (T_c) for second-order magnetic transition [37]. An (30×30) supercell was used, and the simulation for each system lasted for 10^5 loops at each temperature. As shown in Fig. 5(d), T_c is determined to be 130 and 60 K for bilayer CrI_3 on CdSe(0001) and 2D InSe, respectively, while T_c for freestanding CrI_3 monolayer is 40 K from our calculation (45 K in experiment [9]). Encouragingly, the FM order is strengthened by depositing bilayer CrI_3 on bulk semiconductor as T_c increases by up to 3 times.

According to the above discussions, the proximity effect on 2D CrI_3 sheet from the semiconducting substrates originates from the interfacial electronic coupling and charge transfer, which greatly reduces the virtual energy gap and modifies the occupancy of e_g orbitals, leading to enhanced e_g - t_{2g} hybridization and strengthened interlayer ferromagnetic order in bilayer CrI_3 . The interfacial charge transfer is correlated to the work function of the substrate relative to that of CrI_3 . Compared

to the widely adopted approaches like heteroatom doping and functionalization with inherent limitations, depositing 2D magnetic materials on proper semiconducting substrates is a universe strategy to manipulate the spin configuration toward robust ferromagnetism with high Curie temperature for practical applications in spintronics.

IV. CONCLUSION

In summary, we exploited various types of semiconducting substrates to tailor the interlayer spin configuration of bilayer CrI_3 . According to our first-principles calculations and Monte Carlo simulations, the antiferromagnetic ground state of CrI_3 bilayer in high-temperature phase can be transformed into ferromagnetic state when deposited on suitable bulk surfaces or 2D materials. In particular, the (0001) surface of II-VI semiconductors (CdSe, ZnS, and ZnO) form covalent bonds with CrI_3 bilayer and endow it with robust intralayer and interlayer FM order with Curie temperature up to 130 K, much higher than that on 2D substrates with vdW interaction. Such strong proximity effect can be understood by the prominent charge transfer from II-VI semiconductors, leading to carrier doping to the band structure of CrI_3 , which significantly enhances the e_g - t_{2g} hybridization and strengthens the FM nearest-neighbor exchange. These theoretical results provide essential guidance for obtaining high Curie temperature 2D ferromagnets on semiconducting substrates for practical uses.

ACKNOWLEDGMENTS

This work was supported by the National Natural Science Foundation of China (11974068), the Fundamental Research Funds for the Central Universities of China (DUT20LAB110), and the Supercomputing Center of Dalian University of Technology.

There are no conflicts to declare.

-
- [1] K. S. Burch, D. Mandrus, and J.-G. Park, *Nature (London)* **563**, 47 (2018).
 - [2] C. Gong, L. Li, Z. Li, H. Ji, A. Stern, Y. Xia, T. Cao, W. Bao, C. Wang, and Y. Wang, *Nature (London)* **546**, 265 (2017).
 - [3] Z. Wang, I. Gutiérrez-Lezama, N. Ubrig, M. Kroner, M. Gibertini, T. Taniguchi, K. Watanabe, A. Imamoğlu, E. Giannini, and A. F. Morpurgo, *Nat. Commun.* **9**, 2516 (2018).
 - [4] M. Gibertini, M. Koperski, A. Morpurgo, and K. Novoselov, *Nat. Nanotechnol.* **14**, 408 (2019).
 - [5] K. F. Mak, J. Shan, and D. C. Ralph, *Nat. Rev. Phys.* **1**, 646 (2019).
 - [6] B. Huang, G. Clark, E. Navarro-Moratalla, D. R. Klein, R. Cheng, K. L. Seyler, D. Zhong, E. Schmidgall, M. A. McGuire, and D. H. Cobden, *Nature (London)* **546**, 270 (2017).
 - [7] B. Niu, T. Su, B. A. Francisco, S. Ghosh, F. Kargar, X. Huang, M. Lohmann, J. Li, Y. Xu, and T. Taniguchi, *Nano Lett.* **20**, 553 (2019).
 - [8] H. Wang, F. Fan, S. Zhu, and H. Wu, *Europhys. Lett.* **114**, 47001 (2016).
 - [9] B. Huang, G. Clark, D. R. Klein, D. MacNeill, E. Navarro-Moratalla, K. L. Seyler, N. Seyler, M. A. McGuire, D. H. Cobden, and D. Xiao, *Nat. Nanotechnol.* **13**, 544 (2018).
 - [10] P. Li, C. Wang, J. Zhang, S. Chen, D. Guo, W. Ji, and D. Zhong, *Sci. Bull.* **65**, 1064 (2020).
 - [11] M. Grönke, B. Buschbeck, P. Schmidt, M. Valldor, S. Oswald, Q. Hao, A. Lubk, D. Wolf, U. Steiner, and B. Büchner, *Adv. Mater. Interfaces* **6**, 1901410 (2019).
 - [12] K. L. Seyler, D. Zhong, B. Huang, X. Linpeng, N. P. Wilson, T. Taniguchi, K. Watanabe, W. Yao, D. Xiao, and M. A. McGuire, *Nano Lett.* **18**, 3823 (2018).
 - [13] D. Zhong, K. L. Seyler, X. Linpeng, R. Cheng, N. Sivadas, B. Huang, E. Schmidgall, T. Taniguchi, K. Watanabe, and M. A. McGuire, *Sci. Adv.* **3**, e1603113 (2017).
 - [14] D. Zhong, K. L. Seyler, X. Linpeng, N. P. Wilson, T. Taniguchi, K. Watanabe, M. A. McGuire, K.-M. C. Fu, D. Xiao, and W. Yao *et al.*, *Nat. Nanotechnol.* **15**, 187 (2020).
 - [15] M. Ge, Y. Su, H. Wang, G. Yang, and J. Zhang, *RSC Adv.* **9**, 14766 (2019).

- [16] J. Xie, L. Jia, H. Shi, D. Yang, and M. Si, *Jpn. J. Appl. Phys.* **58**, 010906 (2018).
- [17] C. Lin, Y. Li, Q. Wei, Q. Shen, Y. Cheng, and W. Huang, *ACS Appl. Mater. Interfaces* **11**, 18858 (2019).
- [18] Y. Hou and R. Wu, *Sci. Adv.* **5**, eaaw1874 (2018).
- [19] H. Fu, C.-X. Liu, and B. Yan, *Sci. Adv.* **6**, eaaz0948 (2020).
- [20] S. Chen, C. Huang, H. Sun, J. Ding, P. Jena, and E. Kan, *J. Phys. Chem. C* **123**, 17987 (2019).
- [21] H. Li, Y.-K. Xu, K. Lai, and W.-B. Zhang, *Phys. Chem. Chem. Phys.* **21**, 11949 (2019).
- [22] G. Kresse and J. Furthmüller, *Phys. Rev. B* **54**, 11169 (1996).
- [23] G. Kresse and D. Joubert, *Phys. Rev. B* **59**, 1758 (1999).
- [24] J. P. Perdew, K. Burke, and M. Ernzerhof, *Phys. Rev. Lett.* **77**, 3865 (1996).
- [25] S. Grimme, J. Antony, S. Ehrlich, and H. Krieg, *J. Chem. Phys.* **132**, 154104 (2010).
- [26] See Supplemental Material at <http://link.aps.org/supplemental/10.1103/PhysRevMaterials.4.094003> for complementary tables, figures, geometrical structure construction, and description of magnetic model.
- [27] S. W. Jang, M. Y. Jeong, H. Yoon, S. Ryee, and M. J. Han, *Phys. Rev. Mater.* **3**, 031001(R) (2019).
- [28] A. I. Liechtenstein, V. I. Anisimov, and J. Zaanen, *Phys. Rev. B* **52**, R5467(R) (1995).
- [29] G. Henkelman, A. Arnaldsson, and H. Jónsson, *Comput. Mater. Sci.* **36**, 354 (2006).
- [30] P. Anderson, *Phys. Rev.* **79**, 350 (1950).
- [31] J. B. Goodenough, *Phys. Rev.* **100**, 564 (1955).
- [32] J. Kanamori, *J. Phys. Chem. Solids* **10**, 87 (1959).
- [33] D. Soriano, C. Cardoso, and J. Fernández-Rossier, *Solid State Commun.* **299**, 113662 (2019).
- [34] N. Sivadas, S. Okamoto, X. Xu, C. J. Fennie, and D. Xiao, *Nano Lett.* **18**, 7658 (2018).
- [35] T. C. Song, X. H. Cai, M. W. Y. Tu, X. O. Zhang, B. V. Huang, N. P. Wilson, K. L. Seyler, L. Zhu, T. Taniguchi, and K. Watanabe *et al.*, *Science* **360**, 1214 (2018).
- [36] D. R. Klein, D. MacNeill, J. L. Lado, D. Soriano, E. Navarro-Moratalla, K. Watanabe, T. Taniguchi, S. Manni, P. Canfield, and J. Fernandez-Rossier *et al.*, *Science* **360**, 1218 (2018).
- [37] X. Li and J. Yang, *J. Phys. Chem. Lett.* **10**, 2439 (2019).
- [38] R. L. Consigny, III and J. R. Madigan, *Solid State Commun.* **7**, 189 (1969).
- [39] S. Siol, P. Schulz, M. Young, K. A. Borup, G. Teeter, and A. Zakutayev, *Adv. Mater. Interfaces* **3**, 1600755 (2016).
- [40] R. Schlesinger, Y. Xu, O. T. Hofmann, S. Winkler, J. Frisch, J. Niederhausen, A. Vollmer, S. Blumstengel, F. Henneberger, P. Rinke, M. Scheffler, and N. Koch, *Phys. Rev. B* **87**, 155311 (2013).
- [41] R. M. Feenstra, J. A. Stroscio, and A. P. Fein, *Surf. Sci.* **181**, 295 (1987).
- [42] Y. Pan, Y. Wang, M. Ye, R. Quhe, H. Zhong, Z. Song, X. Peng, D. Yu, J. Yang, and J. Shi, *Chem. Mater.* **28**, 2100 (2016).